Gamma-Ray Tracking for High Energy Gamma-Ray Imaging in Pixelated CdZnTe

Daniel Shy, Zhong He

Department of Nuclear Engineering and Radiological Sciences, University of Michigan, Ann Arbor, MI 48109, USA

Abstract

Sequencing gamma-ray interactions within a detector system is an integral component of Compton imaging. In detectors with poor timing resolution compared to the time interval of successive interactions, algorithms which order gamma-ray interactions must be implemented using only energy and position information. This work examines previous algorithms and inspects interaction kinematics to increase the sequencing algorithm's speed and effectiveness. The proposed method, in which the first interaction is assumed to deposit the largest energy, has improved sequencing performance by greater than 20% for full energy gamma ray depositions larger than 1 MeV that do not contain pair-production. In addition, the algorithm shows a decrease in computational costs for sequence reconstruction to allow for better real time reconstruction. Experimental results show an almost twofold increase in the signal to noise ratio (SNR) for simple backprojection images of a ^{22}Na source. Additional measurements of the 2.2 MeV gamma rays from $H^1(n,\gamma)D^2$ neutron capture demonstrates the proposed algorithm's superior performance.

Keywords: Gamma-ray tracking, Compton event reconstruction, 3D position sensitive CdZnTe, event sequencing, Compton kinematics, high energy gamma-ray imaging

1. Introduction

Compton gamma-ray imaging has a multitude of applications in fields ranging from astronomy [1], to medicine [2], to nuclear security [3]. It requires knowledge of the gamma-ray interaction locations and deposited energies, which is sequenced, reconstructed, and then backprojected to estimate the direction of the incident gamma ray. When a gamma ray with energy E_0 enters the detector, it commonly interacts through the following modes: photoelectric absorption, Compton scattering, or pair production. If the photon scatters first and interacts for a total of two or more times, the line between the first two interaction locations creates the axis of the Compton cone with an opening angle derived from the Compton scattering formula. The Compton cone represents the possible directions from which the incident photon originated. The opening angle (Θ) is represented by:

$$\cos(\Theta) = 1 - \frac{m_e c^2 E_1}{E_0(E_0 - E_1)}, \qquad (1)$$

where E_1 is the deposited energy in the first interaction, the electron rest energy is represented by $m_e c^2$, and the incident energy E_0 is either known *a priori* or assumed to be the summation of the observed interactions. Imaging events that did not undergo full energy dispositions will result in an incorrect larger cone opening angle and image artifacts [4]. Full energy peaks are commonly imaged as they have a large probability of full energy deposition. Therefore, partial energy depositions were not included in this study.

The Compton cone is then backprojected onto an image sphere, which intersects it by a ring, and is known as a Compton ring. Combining multiple Compton rings estimate the direction of the emitting source. Different image reconstruction algorithms exist, such as maximum likelihood expected maximization algorithms [5, 6], and direct inverse algorithms, such as filtered backprojection, which deconvolves out detector response [7].

In smaller detectors, where the timing resolution prevents the sequencing of interactions, "sequence reconstruction", or "gamma-ray tracking", algorithms must be implemented to sequence events [8]. This paper explores sequencing events that undergo three-or-more (3+) interactions. To illustrate the importance of sequencing 3+ interaction, a simulation was completed which kinematically models the number of interactions a gamma ray undergoes before being fully attenuated in the detector, neglecting pair-production. Fig. 1a plots the fraction of 3+ events with respect to the total number of imageable events. Already, at 1 MeV, the fraction is close to 50%. Fig. 1b plots the number of interactions as a function of full energy deposition which demonstrates that when exploring higher energies, the number of pixel events slightly increases.

1.1. University of Michigan 4π Compton gamma-ray imager

The current University of Michigan 4π Compton Imager, named Orion Prototype, employs an array of $2 \times 2 \times 1.5$ cm^3 CdZnTe crystals, each with 11×11 pixelated anodes and a planar cathode which can preform high resolution spectroscopy and real time Compton imaging. These detectors can provide the positions of interactions with a spatial resolution of about 0.3 mm in 3-dimensions at 662 keV [9]. The Orion system
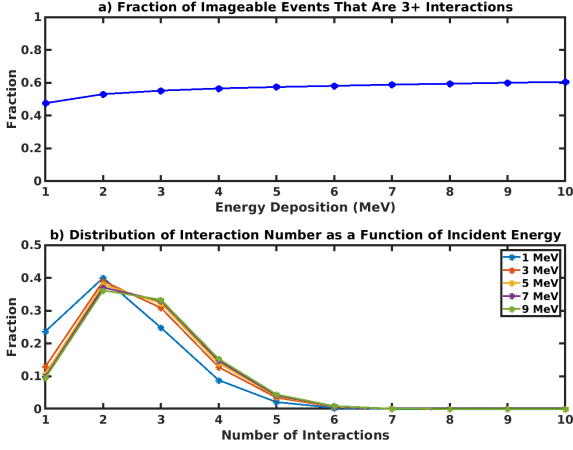
Figure 1: a) Fraction representing the number of 3+ interaction events with respect to the total number of imageable events (2+). b) Distribution of the number of interactions as a function of energy deposited due to kinematic interactions alone. Note that in reality, the distribution would be skewed to favor higher number of interactions due to detector charge sharing and physics effects such as bremsstrahlung.

has an energy resolution of about 0.35% full width at half max (FWHM) at 662 keV using single pixel events, and about 0.5% FWHM for all events, operated at room temperature.

2. Sequence order reconstruction

With 3D-position-sensitive detectors, both the position ($\mathbf{r}_i$) and energy deposited (E_i) of the ith interaction in the sequence are recorded. The following definitions and notation will be used throughout this article. An "interaction" describes a single detectable gamma-ray interaction, while a "sequence", or "event", refer to a collection of interactions that originated from a single incident gamma ray. N represents the number of interactions a gamma ray has undergone in the detector; thus, there are $N!$ possible permutations for each event. For sequence order indexing, the bold numeric indexes represent the chosen sequence order. Capital Roman alphabet designate an order based on decreasing energy and lower case alphabet represents some scrambled sequence. Combined with inferences that could be made from the kinematics of Compton scattering, the techniques presented in the following sections have been developed for events with different numbers of interactions.

The consequences of false sequencing depend on the number of interactions, incident energy, and detector geometry [8]. One artifact that incorrect sequencing will produce is a ring, or halo, around the true source location as well as a decrease in the signal to noise ratio (SNR) of the image, further discussed in Appendix A.

2.1. Two-pixel events

In two pixel events, the sequence has two possibilities of arrangement, either interaction index A then B, or B then A. The current method used is known as simple comparison [10]. In the algorithm, each interaction is checked with a "Compton

Edge Test", which determines if the interaction could have kinematically undergone a Compton scatter. If the interaction fails the test, where its deposited energy is larger than the Compton edge, then it can be inferred that it was a photoelectric absorption and is designated with an index **2**. However, if both interactions have energies lower than the Compton edge, the interaction with the highest energy is assigned an index **1**.

2.2. Three-or-more pixel events

There are several popular methods available to reconstruct three-or-more pixel events, among them, are the deterministic method and Minimum Squared Difference (MSD) technique [10, 11, 12]. The deterministic method simply chooses the sequence with the highest probability of occurrence by calculating the probability of the interaction for each possible sequence permutation with the Klein-Nishina differential cross section and attenuation probabilities. The MSD method, however, assigns a figure of merit (FOM) to each possible sequence by comparing the angle between three interactions ($\theta = \angle \mathbf{r}_a \mathbf{r}_b \mathbf{r}_c$) [13], calculated using the physical locations of interactions and the Compton scattering formula with the following expression [14]:

$$\text{FOM} = \frac{1}{\sqrt{\sigma_{\theta_E}^2 + \sigma_{\theta_R}^2}} e^{-\frac{(\theta_E - \theta_R)^2}{2\left(\sigma_{\theta_E}^2 + \sigma_{\theta_R}^2\right)}}, \quad (2)$$

where θ_E is the angle calculated between the first three interactions using the Compton scattering equation while θ_R is the measured angle. The associated error of the angles is calculated by error propagating the position and energy information of the event and are denoted by σ_{θ_E} and σ_{θ_r} [15]. The sequence with the highest FOM is selected for imaging.

Both methods require calculations for all $N!$ possible sequence permutations. The MSD technique has been shown to outperform the deterministic method in both accuracy and computational cost [16]. This technique can be expanded to 3+ interaction events by summing the FOM for each triplet in the sequence (i.e., in a 4-interaction event: $\text{FOM}_{sequence} = \text{FOM}_{abc} + \text{FOM}_{bcd}$).

3. Kinematics of multiple Compton scatters

The Compton-scattering differential angular cross section is described by the Klein-Nishina (KN) formula [17]. It computes the angular likelihood of scattering a photon into a solid angle $d\Omega$ in scattering direction θ with the expression:

$$\frac{d\sigma}{d\Omega} = \frac{r_0^2}{2} \left\{ \frac{1}{[1 + \alpha(1 - \cos\theta)]^2} \left[1 + \cos^2\theta + \frac{\alpha^2(1 - \cos\theta)^2}{[1 + \alpha(1 - \cos\theta)]} \right] \right\}, \quad (3)$$

where $r_0 = e^2/m_e c^2$ represents the classical radius of the electron and $\alpha = E_0/m_e c^2$.

3.1. Probability of electron recoil energy calculation using Klein–Nishina cross sections

To explore the differential cross section for a Compton scatter to produce a recoil electron in an interval $[T, T + dT]$, the
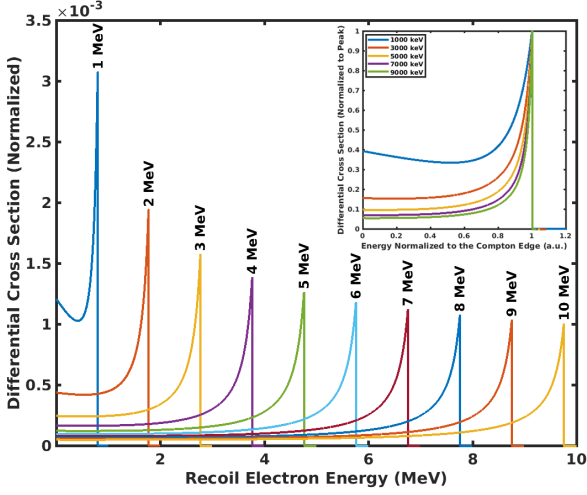
Figure 2: Klein-Nishina differential cross section as a function of recoil electron energy (T) for different incident energy gamma rays. The curves are normalized with the total cross section for scattering at that incident energy. Inset are the cross sections for different incident energies with the Compton continuum normalized to the Compton edge.

following Jacobian coordinate transform is applied:

$$\frac{\mathrm{d}\sigma}{\mathrm{d}T} = \frac{\mathrm{d}\sigma}{\mathrm{d}\Omega}\left[\frac{\mathrm{d}\Omega}{\mathrm{d}\theta}\frac{\mathrm{d}\theta}{\mathrm{d}T}\right], \tag{4}$$

The expression, $\mathrm{d}\Omega/\mathrm{d}\theta = 2\pi\sin\theta$, is obtained from the definition of the solid angle differential. The electron recoil energy is defined as $T = E_0 - E_1' = E_0\frac{\alpha(1-\cos\theta)}{1+\alpha(1-\cos\theta)}$, where E_1' represents the energy of the photon after the first scatter. It can be rearranged and differentiated to result in $\mathrm{d}\theta/\mathrm{d}T$. The final expression in terms of Eq. 3 is:

$$\frac{\mathrm{d}\sigma}{\mathrm{d}T} = \frac{2\pi m_0 c^2}{[E_1']^2}\frac{\mathrm{d}\sigma}{\mathrm{d}\Omega}. \tag{5}$$

The shape of the KN cross section changes as a function of incident energy which shapes the Compton continuum [18]. Fig. 2 shows the shape of the continuum for different incident energies. Note that in practice, the shape of the continuum is affected by the geometry of the detector and is blurred by detector response. When comparing the different continua, the curves become more asymmetric and biased towards higher electron recoil energies as the incident gamma-ray energy increases. This can be seen in the graph inset in Fig. 2, which shows the cross sections normalized to the Compton edge. In other words, as the incident gamma-ray energy enlarges, the distribution of the produced recoil electrons will be skewed left, where the median is greater than the mean.

3.2. Probability that the 1st interaction deposits the largest energy in the sequence

The shape of the Compton continuum, as shown in Fig. 2, can explain the fraction of two-interaction events in which the first interaction has a larger deposited energy than the second interaction, ($E_1 > E_2$). The fraction of events in which the first

interaction deposits the most energy in the sequence is represented by the First-Is-Largest (FIL) fraction. The FIL fraction for a two-interaction event within an infinitely large detector is described in Eq. 6, where KN(ϵ) represents the Klein–Nishina differential cross section for energy ϵ, and CE is the Compton edge for incident energy E_0. The lower limit ($\frac{E_0}{2}$) in Eq. 6 is chosen, since the event must be FIL if the first interaction deposits an energy $\frac{E_0}{2}$ or higher.

If an interaction deposits less than $E_1 = \frac{E_0}{N}$, where N is the number of interactions, it could never be a FIL event. Therefore, Eq. 6 is used to describe the lower bound of the FIL ratio. For 3+ interaction events, $E_1 = \frac{E_0}{N}$ is used for the lower integral limit of the FIL upper bound ratio since it may still produce an FIL event. This can be proven by first defining the variable f_i, which is the deposited energy in the ith interaction as a fraction of E_0, ($E_2 = f_2 E_0$), and note that $\sum_{i=2}^{N} f_i = 1 - f_1$. Next, the fraction f_1 is found where $E_1 > E_i\ \forall\ i \in \{2, \dots, N\}$, or where $\frac{E_i}{E_1} = \frac{f_i E_0}{f_1 E_0} = \frac{f_i}{f_1} < 1$. Then, the summation of $\frac{f_i}{f_1}$ is taken, which yields $\sum_{i=2}^{N} \frac{f_i}{f_1} = \frac{1}{f_1}\sum_{i=2}^{N} f_i < \sum_{i=2}^{N} 1 = N - 1$. Solving for f_1 yields $f_1 > \frac{1}{N}$ for the fraction of E_0, or $E_1 > \frac{E_0}{N}$, to deposit in the first interaction and still result in an FIL event. Therefore, Eq. 7 is defined as the upper bound for the FIL fraction, or $P(E_1 > E_i)\ \forall\ i \in \{2, \dots, N\}$. Fig. 3 plots both the bounds for the FIL fraction in an infinite detector for different number of interactions.

$$\text{FIL}(E_0)_{lower\,bound} = \frac{\int_{\frac{E_0}{2}}^{CE} \text{KN}(\epsilon)\mathrm{d}\epsilon}{\int_{0}^{CE} \text{KN}(\epsilon)\mathrm{d}\epsilon} \tag{6}$$

$$\text{FIL}(E_0)_{upper\,bound} = \frac{\int_{\frac{E_0}{N}}^{CE} \text{KN}(\epsilon)\mathrm{d}\epsilon}{\int_{0}^{CE} \text{KN}(\epsilon)\mathrm{d}\epsilon} \tag{7}$$
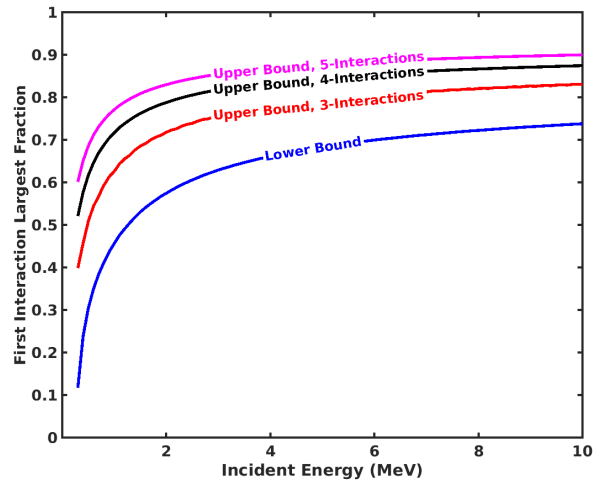

Figure 3: FIL fraction limits for events in which the first interaction deposited the largest energy in the sequence for various incident energies in an infinite detector.

We therefore modify the standard MSD algorithm to assume that the first interaction is the largest (FIL) followed by the stan-

3

dard MSD figure of merit calculations for the subsequent interactions. This technique is referred herein as the "FIL-MSD" algorithm.

It is natural to conclude from the FIL fraction that the subsequent interactions will deposit the next highest energies. This is what is referred to as ABC sequencing, but our results have shown it to be inferior to FIL-MSD as the ABC sequence does not have a high probability of occurrence. After the first interaction, the gamma ray loses a significant amount of energy where the scattered gamma-ray does not have enough energy to continue to produce an FIL event. Instead, a "Complex Comparison" method was developed where an ABC or ACB sequence is chosen based on the energy of the scattered gamma-ray ($E_1' = E_0 - E_1$), where the first interaction is assumed to be FIL. The next two interactions are sequenced using the simple comparison technique. This technique has shown better results than MSD but lower efficiency than FIL-MSD. Nevertheless, Complex Comparison is useful for detector systems that have poor position resolution which degrades the MSD performance.

4. Monte Carlo simulation

4.1. Simulation parameters

Simulations using GEANT4 were performed to model the behaviour of the Orion prototype [19]. Multiple gamma-ray interactions under the same pixel anode were treated as a single site interaction. Since it is not possible to Compton image an event if the first interaction results in a pair-production, the pair production physics package was not included in the program physics lists for computational considerations. The fraction of events that have a pair production event following a Compton scatter interaction is negligible for full energy deposition events. Presenting pair production data may be misleading. Data generated for the sequencing studies did not include electron thermalization, or the loss energy of the electron in the medium, and therefore did not include the triggering of multiple pixels by a single interaction. Another simulation was performed to study the movement of the recoil electron traversing the material to quantify the associated position blur from the electron cloud size. The simulated data that was created for the sequencing study modeled 1e8 gamma rays that were randomly produced in various directions.

4.2. Production of realistic data by estimating position resolution

A major factor in position resolution is the size of the electron cloud produced by the recoiled electron. Since larger deposited energies produce larger electron clouds, the induced signal on each pixel will significantly change and affect the position reconstruction. The electron clouds were modeled in GEANT4 by tracking the electron paths. The cloud's size is defined as the distance between the largest separation between two electrons as done by Kim *et. al* [20]. Fig. 4 shows the electron cloud distribution as a function of deposited energy with a log-log fit shown in Eq. 8.
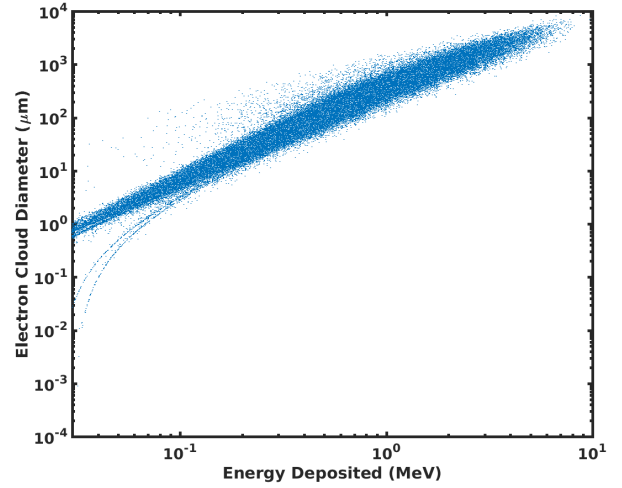

Figure 4: Electron cloud size as a function of single-site deposited energy in CdZnTe. Note that the log-log fit could be simplified to $Diameter = 398.1E_{dep}^{1.8}$.

$$Y = 1.8X + 2.6,$$
$$Y = \log_{10} \text{diameter } (\mu m), \quad (8)$$
$$X = \log_{10} \text{energy (MeV)}.$$

The model does not show the decrease of position resolution of low-energy depositions caused by the decrease in induced transient signals, compared to the readout electronic noise, and is not considered in this study.

5. Results and discussion

5.1. Simulated algorithm performance

The simulated data were analyzed using the different algorithms. The FIL-MSD algorithm is compared to the standard MSD algorithm in Fig. 5 and shows the percentage increase in accuracy as a function of the incident gamma-ray energy. The evaluation of the algorithm only considered events in which the gamma rays deposited all their energies in the crystal. The results show a greater than 20% increase in accuracy for FIL-MSD over standard MSD for 3+ interaction events that have energies higher than 1 MeV. The FIL-MSD algorithm is also more accurate for energies lower than 1 MeV and does better than MSD down to energies as low as 350 keV. Therefore, in cases where the incident gamma ray deposits less than 350 keV, the standard MSD could be implemented rather than FIL-MSD. The exact threshold for which FIL-MSD is inferior depends on detector shape.

A ^{22}Na source was simulated with GEANT4, modeling the source 1 meter away from the detector, and with no background. To show the benefit of the algorithm, pair-production physics were not considered in this section. Fig. 6a-c present simple backprojection images using the a) true sequence, b) MSD, and c) FIL-MSD algorithms with a total of 100,000 events consisting of 3, 4, 5 interactions. From the figure, it is obvious that the
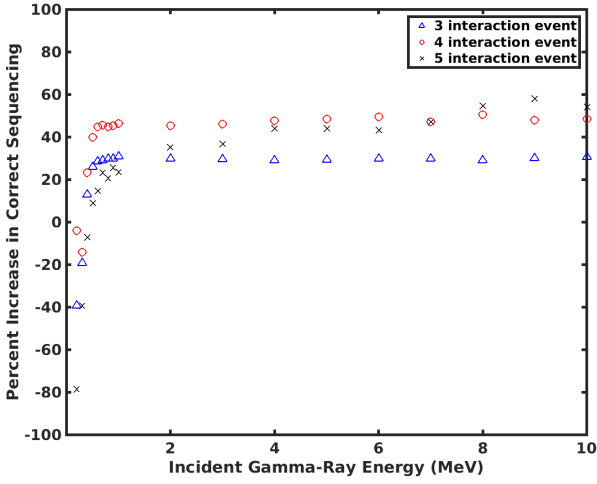
4

Figure 5: Percentage increase in accuracy when comparing the FIL-MSD and MSD algorithms for simulated events.

image acutance has increased in the FIL-MSD algorithm and that the halo around the hotspot arises from false sequenced events. Table 1 displays the signal-to-noise (SNR) ratios of the images as well as characteristics of the point spread function (PSF). The SNR grew by a factor of 1.76 when comparing FIL-MSD with standard MSD. The increase in FWHM of the PSF is discussed in greater detail in Sec. 5.4.

Table 1: Table of the associated FWHM and SNR of each SBP image using the two different algorithms. FWHM was measured by fitting a double Gaussian to the axial image slice. The SNR was calculated by (I/σ) with max value in the ROI (I) and the (σ) representing the standard deviation of the image outside the ROI. Data within 3σ was chosen as the ROI for the image. The SNR calculation for 'True' was omitted as it is not appropriate to calculate the noise of an image with no sequencing noise.

Algorithm	θ FWHM	ϕ FWHM	SNR (I/σ)
Simulated Data			
True	34.3	34.3	$\sim$
MSD	26.7	31.1	24.2
FIL-MSD	30.8	30.1	42.7
Experimental Data			
MSD	25.6	31.5	23.9
FIL-MSD	31.7	32.5	45.8

5.2. Computation cost comparison

The computational cost is of interest, especially for higher energy gamma rays, as they are likely to have a larger number of interactions. The MSD algorithm requires a FOM to be calculated for every $N!$ permutation. However, by assuming FIL, the number of FOM calculations is decreased to $(N-1)!$ calculations, theoretically decreasing the computation by a factor of N. Table 2 shows the performance of each algorithm by analyzing the average time needed to reconstruct each event. It can be seen that the FIL-MSD computes the sequence faster than the standard MSD.
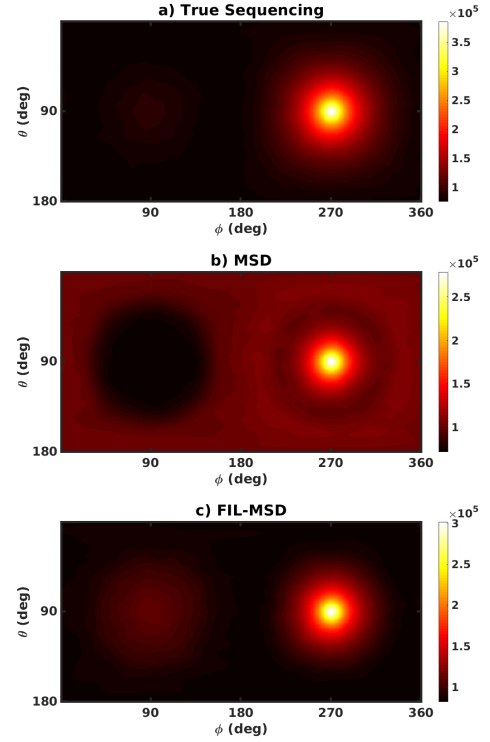

Figure 6: Simple backprojection images of a simulated ^{22}Na source using the a) true, b) MSD, and c) FIL-MSD sequencing algorithm. The image uses only 3, 4, and 5 pixel for a total of 100,000 events. The simulation consisted of an isotropic source defined to be 1 meter away from the detector.

Table 2: Average computational time to sequence an event.

N	MSD (μs)	FIL-MSD (μs)	$t_{FIL-MSD}/t_{MSD}$
Three	12.5	6.5	2.1
Four	49.9	15.1	3.3
Five	492.1	106.6	4.9

5.3. Compton image reconstruction with experimental results

The University of Michigan Orion Prototype system measured and imaged a 45 μCi ^{22}Na gamma-ray source from 85 cm away using one CdZnTe Crystal. A simple backprojection (SBP) image using the standard MSD algorithm is displayed in Fig. 7a which used 8,600 photopeak events of only 3, 4, 5 interaction events. The visible ring and halo background artifacts in Fig. 7b arise from incorrectly sequenced events. Some artifacts may arise from background. However, since imaging was done using the photopeak, room return would have down scattered and not added to the image. Fig. 7b displays the reconstructed image using the FIL-MSD algorithm. It has a signal-to-noise ratio (SNR) 1.92 times better than that of the MSD image.

The FIL-MSD method creates an image artifact 180° from the true source location. This is due to the point spread function of scatters nearing 90° as well as missequenced events. The SNR and the associated FWHM of the point spread function
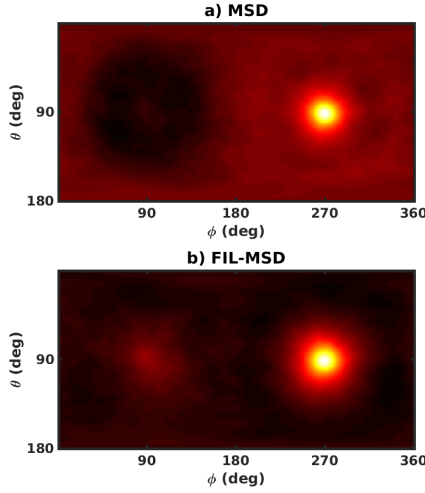
Figure 7: Simple backprojection images using only 3,4, and 5 pixel events of a ^{22}Na at 85 *cm* away from the detector, (a) using the standard MSD sequence reconstruction, (b) using FIL-MSD algorithm. Both the images were normalized to the peak of the MSD reconstruction.

Figure 8: Point spread functions (PSF) of different sequencing algorithms using the simulated ^{22}Na data. a) The polar slice along the hot spot while b) plots the azimuthal. All curves were baseline subtracted with the minimum value. Note the two humps created from missequenced events by MSD left and right of the hotspot.

(PSF) are tabulated in Table 1. The table shows an increase in the FWHM when comparing the FIL-MSD with the MSD reconstruction, which is most likely a result of the event type reconstructed.

5.4. *Discussion on the angular resolution (FWHM) calculation*

The increase of the FWHM in the PSF for FIL-MSD may raise some concerns, but could also provide a positive indicator of the sequencing efficiency of the algorithm. First, since different types of events have different responses (the PSF changes for different scatter angles), one can select events that produce high resolution images regardless of sequencing methods which produce a smaller FWHM. Using simulated data and the correct sequencing (Fig. 6a), a larger FWHM was reconstructed when compared to MSD and FIL-MSD. As all events are sequenced and used in the 'True' image, both high and low resolution events contribute to the image. The MSD/FIL-MSD algorithms produce a slightly smaller FWHM as they correctly sequence more high resolution events. In other words, MSD/FIL-MSD correctly sequences a subset of all events that are high resolution which artificially decreases the FWHM. We can further explore these phenomena by plotting the azimuthal and polar slices of the images (Fig. 8). The figure clearly shows that the 'True' sequencing image has the widest PSF. FIL-MSD sequences a broader range of events with higher efficiency, so event cuts could be implemented to isolate high resolution events.

5.5. *Imaging the 2.2 MeV gamma rays off neutron capture on hydrogen*

It was also useful to image the 2.2 MeV gamma rays from the neutron capture on hydrogen and investigate the imaging performance of the new algorithm. This is especially of interest for security and astro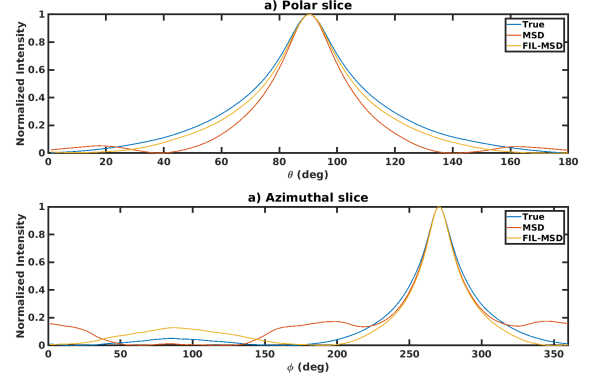nomical applications as it could indicate the presence of hydrogen when searching for explosives [21], or water on locations such as the moon [22]. In the experiment, using a 3×3 crystal Orion detector system, a 2.8 *mCi* ^{252}Cf, emitting 1.2e7 neutrons/s, was set in the middle of a $1^{\varnothing}$ ft $\times$ 1 ft polyvinyl cylinder tube. The source was placed 105 *cm* away from the cathode with all other detector faces shielded with lead and borated polyethylene to prevent contamination from room return.

Events that have a combination of interactions that sum up to a deposited energy of 511 ± 4 keV were removed as a means to discard pair-production events. Since electron-positron annihilation emit two photons near 511 keV gamma rays, it is a good indication that a pair-production event occurred. Fig. 9a-b present images of a 2 hour measurement of the source using only 3, 4, and 5 pixel events with the MSD and FIL-MSD algorithm respectively. All the possible opening cone angles (Θ from Eq. 1) were used in those reconstructions. Fig. 9a shows significant artifacting from small angle cones, which do not backproject onto the true source direction. This is probably due to incorrectly sequenced events. Events that were reconstructed with an opening angle of less than 25°, sequenced with the MSD algorithm, are shown in Fig. 9c, where a hotspot is not clearly visible. Using that same data set, Fig. 9d was produced with the FIL-MSD algorithm, which shows a clear hotspot that was not visible in the MSD sequenced image. This shows that FIL-MSD has a higher sequencing efficiency than standard MSD. Re-sequenced and incorrect sequencing are discussed in Appendix A.

6. Conclusion

The proposed FIL-MSD algorithm has shown at least a 20% increase in correct sequencing of events with full energy deposition. The increased in performance was analyzed for incident gamma rays above 1 MeV in simulated events that produce 3+ pixel events with omitted pair-production. By choosing the first interaction to be the largest in the sequence, the computational
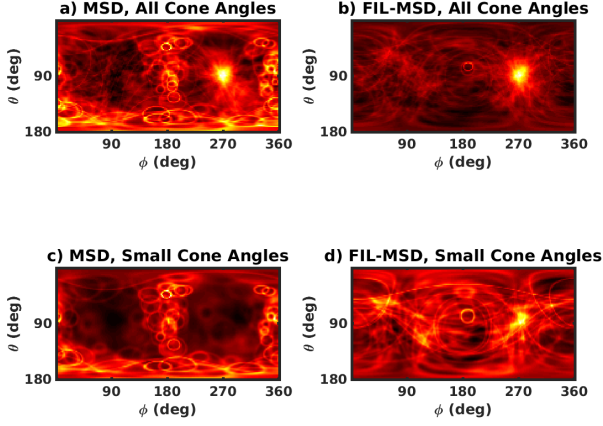
Figure 9: Simple backprojection image of a 2.2 MeV source using (a) the standard MSD sequence reconstruction and (b) FIL-MSD algorithm. The images use all possible cone opening angles. An opening angle upper threshold of $\Theta < 25°$ was set for (c) and the same dataset was used with the FIL-MSD algorithm for (d).

time required to reconstruct events has also decreased substantially.

This technique has also increased the signal-to-noise ratio of the reconstructed Compton images. Experimental results, using a ^{22}Na source, show an almost two-fold increase in SNR. The new sequencing technique did, however, reconstruct images with a higher FWHM. This is due to the fact that FIL-MSD has a broader range of events that is correctly sequenced. Therefore, FIL-MSD sequences both high and low quality events whereas MSD tends to correctly sequence fewer low quality events. This discrepancy can be resolved by applying event cuts that artificially improve the angular resolution of the PSF.

Appendix A. Additional image analysis on incorrect sequencing

This appendix illustrates the image artifacts generated by incorrect sequencing and the advanced sequencing efficiency of FIL-MSD. This is done by reconstructing some of the MSD's sequenced events with FIL-MSD to yield an image with higher signal to noise. Similar to Fig. 9, where the small angle components reconstructed by MSD were isolated and re-sequenced with FIL-MSD, the same was completed with the ^{22}Na measurement and presented in Fig. A.10. Fig. A.10a-b are images that make use of all the data, whereas (c) displays the isolated low opening angle components which is then re-sequenced with FIL-MSD to produce (d). Opening angles above 25° using MSD are shown in (e) and re-sequenced with FIL-MSD in (f). The same is presented in Fig. A.11 for a 2.2 MeV source.
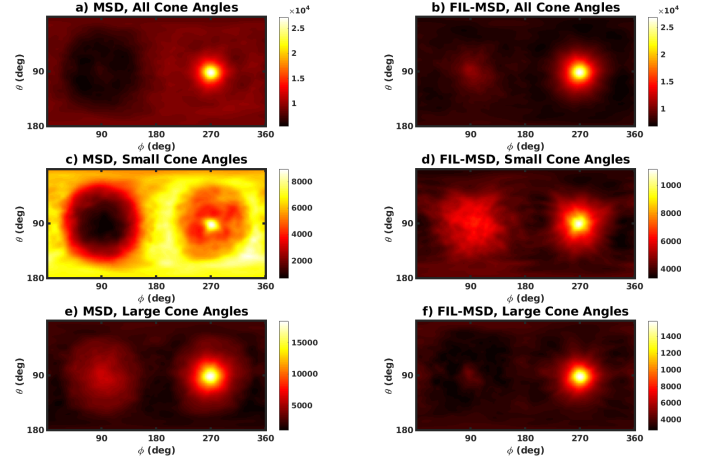
Figure A.10: The left column represents events sequenced using the MSD algorithm for an ^{22}Na while the right column is sequenced with FIL-MSD . Different event cuts were performed on each row regarding the reconstructed scattering angle. The right column displays the re-sequenced events imaged by the left column. Therefore, the left and right columns display the same data just sequenced with different algorithms.
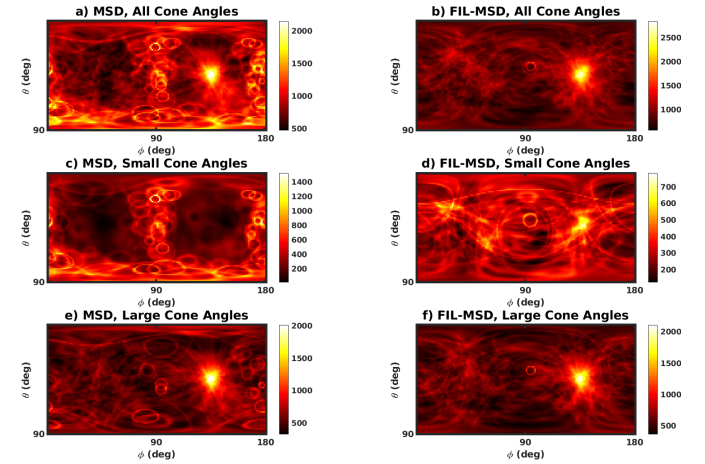

Figure A.11: Experimental measurement, as displayed in Fig. A.10, using a 2.2 MeV source.

References

[1] V. Schonfelder, R. Diehl, G. G. Lichti, H. Steinle, B. N. Swanenburg, A. J. M. Deerenberg, H. Aarts, J. Lockwood, W. Webber, J. Macri, J. Ryan, G. Simpson, B. G. Taylor, K. Bennett, M. Snelling, The imaging compton telescope comptel on the gamma ray observatory, IEEE Transactions on Nuclear Science 31 (1) (1984) 766–770.

[2] E. Draeger, D. Mackin, S. Peterson, H. Chen, S. Avery, S. Beddar, J. C. Polf, 3d prompt gamma imaging for proton beam range verification, Physics in Medicine & Biology 63 (3) (2018) 035019.

[3] K. Vetter, R. Barnowksi, A. Haefner, T. H. Joshi, R. Pavlovsky, B. J. Quiter, Gamma-ray imaging for nuclear security and safety: Towards 3-d gamma-ray vision, Nuclear Instruments and Methods in Physics Research Section A: Accelerators, Spectrometers, Detectors and Associated Equipment 878 (2018) 159 – 168.

[4] J. Chu, Advanced Imaging Algorithms with Position-Sensitive Gamma-Ray Detectors, Ph.D. thesis, University of Michigan (2018).

[5] W. Wang, C. G. Wahl, J. M. Jaworski, Z. He, Maximum-likelihood deconvolution in the spatial and spatial-energy domain for events with any number of interactions, IEEE Transactions on Nuclear Science 59 (2) (2012) 469–478.

[6] C. E. Lehner, Z. He, F. Zhang, 4 pi compton imaging using a 3-d position-sensitive cdznte detector via weighted list-mode maximum likelihood, IEEE Transactions on Nuclear Science 51 (4) (2004) 1618–1624.

[7] J. Chu, M. Streicher, J. A. Fessler, Z. He, Unbiased filtered backprojection in 4π compton imaging with 3d position sensitive detectors, IEEE Transactions on Nuclear Science 63 (6) (2016) 2750–2756.

[8] C. E. Lehner, Z. He, Image artifacts resulting from gamma-ray tracking algorithms used with compton imagers, in: IEEE Symposium Conference Record Nuclear Science 2004., Vol. 3, 2004, pp. 1599–1603 Vol. 3.

[9] Y. Zhu, S. E. Anderson, Z. He, Sub-pixel position sensing for pixelated, 3-d position sensitive, wide band-gap, semiconductor, gamma-ray detectors, IEEE Transactions on Nuclear Science 58 (3) (2011) 1400–1409.

[10] D. Xu, Gamma-ray imaging and polarization measure using 3-d position-sensitive CdZnTe detectors, Ph.D. thesis, University of Michigan (2006).

[11] R. A. Kroeger, W. N. Johnson, J. D. Kurfess, B. F. Phlips, E. A. Wulf, Three-Compton Telescope: Theory, Simulations, and Performance, IEEE Transactions Nuclear Science 49 (4) (2002) 1887–1892.

[12] I. Lee, Gamma-ray tracking detectors, Nuclear Instruments and Methods in Physics Research Section A: Accelerators, Spectrometers, Detectors and Associated Equipment 422 (1) (1999) 195 – 200.

[13] N. Dogan, D. Wehe, G. Knoll, Multiple compton scattering gamma ray imaging camera, Nuclear Instruments and Methods in Physics Research Section A: Accelerators, Spectrometers, Detectors and Associated Equipment 299 (1) (1990) 501 – 506.

[14] C. Wahl, Imaging, Detection, and Identification Algorithms for Position-Sensitive Gamma-Ray Detectors, Ph.D. thesis, University of Michigan (2011).

[15] C. E. Lehner, 4-pi Compton imaging using a single 3-d position sensitive CdZnTe detector, Ph.D. thesis, University of Michigan (2004).

[16] C. L. Thrall, C. G. Wahl, Z. He, Performance of five-or-more-pixel event sequence reconstruction for 3-D semiconductor gamma-ray-imaging spectrometers, in: 2008 IEEE Nuclear Science Symposium Conference Record, 2008, pp. 1299–1301.

[17] O. Klein, Y. Nishina, Über die streuung von strahlung durch freie elektronen nach der neuen relativistischen quantendynamik von dirac, Zeitschrift für Physik 52 (11) (1929) 853–868.

[18] D. Maeder, R. Muller, V. Wintersteiger, Über die Linienform monochromatischer γ–Strahlungen im Szintillationsspektrographen. (German) [on the line shape of monochromatic gamma radiation in a scintillation spectrograph], Helvetica Physica Acta Vol: 27.

[19] S. Agostinelli et al., Geant4a simulation toolkit, Nuclear Instruments and Methods in Physics Research Section A: Accelerators, Spectrometers, Detectors and Associated Equipment 506 (3) (2003) 250 – 303.

[20] J. C. Kim, S. E. Anderson, W. Kaye, F. Zhang, Y. Zhu, S. J. Kaye, Z. He, Charge sharing in common-grid pixelated cdznte detectors, Nuclear Instruments and Methods in Physics Research Section A: Accelerators, Spectrometers, Detectors and Associated Equipment 654 (1) (2011) 233 – 243.

[21] J. Rigelsford, Detection of explosives and landmines: Methods and field experience, Sensor Review 23 (4) (2003) 365–366.

[22] W. C. Feldman, D. J. Lawrence, R. C. Elphic, B. L. Barraclough, S. Maurice, I. Genetay, A. B. Binder, Polar hydrogen deposits on the moon, Journal of Geophysical Research: Planets 105 (E2) (2000) 4175–4195.